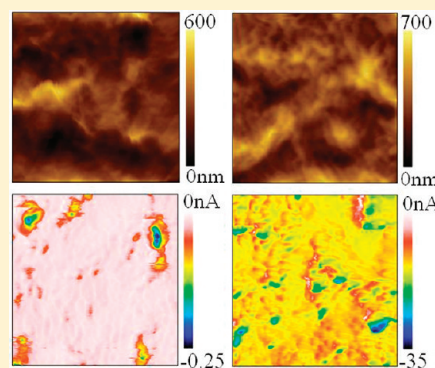


Correlating Humidity-Dependent Ionically Conductive Surface Area with Transport Phenomena in Proton-Exchange Membranes

Qinggang He, Ahmet Kusoglu, Ivan T. Lucas, Kyle Clark, Adam Z. Weber, and Robert Kostecki*

Environmental Energy Technologies Division, Lawrence Berkeley National Laboratory, 1 Cyclotron Road, Berkeley, California 94720, United States

ABSTRACT: The objective of this effort was to correlate the local surface ionic conductance of a Nafion 212 proton-exchange membrane with its bulk and interfacial transport properties as a function of water content. Both macroscopic and microscopic proton conductivities were investigated at different relative humidity levels, using direct-current voltammetry and current-sensing atomic force microscopy (CSAFM). We were able to identify small ion-conducting domains that grew with humidity at the surface of the membrane. Numerical analysis of the surface ionic conductance images recorded at various relative humidity levels helped determine the fractional area of ion-conducting active sites. A simple square-root relationship between the fractional conducting area and observed interfacial mass-transport resistance was established. Furthermore, the relationship between the bulk ionic conductivity and surface ionic conductance pattern of the Nafion membrane was examined.



1. INTRODUCTION

Research in proton-exchange-membrane fuel cells (PEMFCs) has undergone exponential growth over the past decade.^{1–8} The PEM is a critical component for PEMFCs, and it functions as a reactant separator while providing an ionic pathway for proton transport.^{7–9} Nafion, developed by DuPont, is still the most prominent PEM material for PEMFCs and other related technologies. Nafion is a perfluorinated polymer with ether side chains terminated with sulfonic acid groups.^{8,10} When in contact with water, in either liquid or vapor form, Nafion swells and undergoes nanophase separation as the hydrophilic water-filled domains form via solvation of the sulfonic acid groups.^{8,11–14} Once the protons dissociate from the sulfonic acid groups, they move through the water-filled pathways. These phenomena are critical for high membrane proton conductivity and high PEMFC power density.^{15,16}

A wealth of analytical techniques have been used to obtain morphological and structural information about Nafion, including X-ray and neutron scattering,^{13,14,17–22} electron microscopy,²³ atomic force microscopy (AFM),^{24–27} numerical modeling,^{28,29} etc. Numerous studies of the ionic conductivity of Nafion have been reported in the literature. Slade et al.³⁰ determined that ionic conductivity is a function of different orientations of the ionic clusters formed in the cast membrane. Anantaraman et al.³¹ adopted a coaxial probe technique to show that the ionic conductivity of Nafion 117 is nonlinear with regard to water content. Peckham et al. examined sulfonated PEMs and found that the differences in proton conductivity were mainly due to differences in effective proton mobility and acid concentration.^{32,33}

In addition to the bulk ionic conductivity, the surface properties of PEMs play a critical role in PEMFC performance.^{34,35}

In fact, the electrode must be in direct contact with ionic channels on the solid-membrane electrolyte to reduce the interfacial contact resistances between cell components, which together with electrical contact resistances contribute to the overall impedance of the cell. In addition, the surface structure can affect water absorption into the membrane and influence the rate of mass-transfer processes and thereby limit PEMFC performance. Contact angle measurements³⁶ and AFM imaging^{37,38} showed that the surface of the PFSA membrane is predominantly hydrophobic or nonwetting, especially at low relative humidity (RH) levels.

Electrochemical scanning probe techniques are very effective for simultaneous imaging of the surface structure and local distribution of active ion-conducting channels in ion-exchange membranes.^{15,39,40} A conductive STM or AFM probe that is polarized by a potentiostat or voltage bias controller allows simultaneous real-time imaging of both the surface morphology and electrochemical activity.^{41–44} O'Hayre et al.⁴³ obtained impedance-modulus and phase images of Nafion as a function of relative humidity. Proton conductance variation on the Nafion surface was mapped by Zhu et al.,^{40,45} using current-sensing atomic force microscopy (CSAFM). The surface pattern of the hydrophilic paths and their dynamic behavior on the surface of the Nafion membrane were revealed and characterized from the time-resolved ionic conductivity mapping by CSAFM.⁴⁶ Grazing-incidence small-angle X-ray scattering (GISAXS) studies of Nafion confirmed the hydrophobic nature of the membrane surface vs water vapor.^{26,27} In marked contrast, the surface of a

Received: June 29, 2011

Revised: August 27, 2011

Published: September 07, 2011

liquid-equilibrated membrane was found to be completely hydrophilic or wetting.^{26,27}

The effect of mass transfer resistance at the membrane/vapor interface on the water-transport mechanism in Nafion has been investigated using steady-state and transient diffusion measurements.^{47–52} The interfacial resistance was shown to be the limiting step for water transport in thinner membranes (less than 25 μm) at lower temperatures (25 $^{\circ}\text{C}$)^{49,51} and at high relative humidity.⁵² Interestingly, Zhao et al.⁵² reported RH-independent interfacial resistance, whereas Kienitz et al.⁵³ reported a decrease in mass-transport coefficient with increasing RH. However, the extent to which interfacial resistance controls the water transport is still under debate due to the variety of measurement techniques and data analysis methods used.

In this work, we examine the Nafion 212 membrane bulk ionic conductivity and local, surface ionic conductance as a function of relative humidity and membrane water content.

2. EXPERIMENTAL SECTION

2.1. Bulk Conductivity Measurements. The bulk ionic conductivity of the membrane was measured with an in-plane four-probe technique using a BekkTech BT-112 conductivity cell. The in-plane probe cell configuration consists of two Pt outer electrodes that supply the current to the sample and two Pt inner electrodes that measure a voltage drop that is due only to ionic conduction. The membrane sample was cut to 1 cm wide by 3 cm long and loaded into the conductivity cell, which was then assembled into Fuel Cell Technologies hardware. Temperature, pressure, and relative humidity were controlled using a fuel-cell test system (model 850E, Scribner Associates, Inc.). The sample was conditioned at room temperature for 2 h at 25% RH followed by a series of steps in RH value (25%, 30%, 40%, 50%, 60%, 70%, 80%, 90%, and 95%), with each step of 30 min duration (operating parameters: 100 kPa_a, 25C, 1 L/min total N₂ gas flow). Humidity was controlled by mixing wet and dry H₂ gases. Prior to the membrane ionic conductivity measurements, the cell was allowed to equilibrate for 30 min at each RH. DC cyclic voltammetry was performed to determine the membrane bulk resistance. The potential was swept from 0.1 to -0.1 V at 5 mV/s using a Reference 600 Potentiostat/Galvanostat/ZRA (Gamry Instruments). The membrane resistance was determined from the slope of the resulting voltammogram using Gamry Analysis software.

2.2. Water Uptake. The water uptake of the membrane as a function of humidity was determined using a dynamic-vapor-sorption (DVS) analyzer (Surface Measurement Systems). The sample was first equilibrated at 0% RH at $T = 120$ $^{\circ}\text{C}$ for two hours to remove any residual water in the membrane and determine the initial weight of the sample. Then, the membrane was humidified via incremental RH steps of 10% up to 95%. The membrane was equilibrated at each RH step for 2 h to determine its overall weight and water weight W . Water content λ , which represents the number of water molecules per sulfonic acid group,³⁶ is determined by

$$\lambda(\text{RH}) = \frac{W(\text{RH}) - W_{\text{dry}}}{W_{\text{dry}}} \frac{\text{EW}}{18} \quad (1)$$

where EW is the equivalent molar weight of the membrane, i.e., 1100 g/mol for Nafion 212.

2.3. CSAFM Measurements. The CSAFM experimental setup is shown in Figure 1. A commercial AFM system (model 5500,

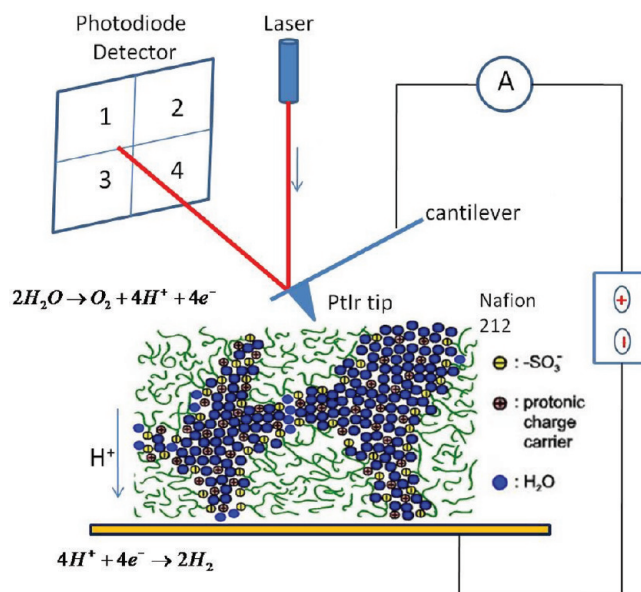


Figure 1. Illustration of the setup for CSAFM measurement with Nafion 212.

Agilent) was equipped with a tip–sample voltage bias circuit capable of sensing currents as low as 1 pA. A conductive, PtIr-coated silicon tip ($k = 1.2\text{--}29$ N/m, Nanosensors) was applied in contact mode and served as the AFM probe to image the morphology of the membrane sample and as the nanoelectrode to probe local surface ionic conductance. During the CSAFM measurements, a DC voltage bias was applied between the AFM tip and the Pt membrane sample holder. Upon DC polarization, H₂ and O₂ evolution reactions took place on the Pt sample holder and the AFM Pt/Ir tip, respectively. The protons generated locally at the tip travel across the membrane and are reduced to form hydrogen at the Pt membrane sample holder. All AFM experiments were performed at room temperature in an environmental chamber filled with air at 30%, 51%, 65%, 77%, and 84% RH levels, which were established using saturated salt solutions of calcium chloride, potassium nitrite, sodium nitrite, sodium nitrate, and potassium chloride, respectively.

3. RESULTS AND DISCUSSION

3.1. Bulk Ionic Conductivity Measurements. Measurements of the bulk ionic conductivity of Nafion 212 were carried out at room temperature at RH levels ranging from 25% to 95%. Consequently, the bulk conductivity (κ) of Nafion 212 can be calculated using the direct-current voltammetry fit data according to

$$\kappa = \frac{L}{R \cdot A} = \frac{L}{R \cdot W \cdot T} \quad (2)$$

where L , W , and T are the length (0.42 cm), width (1.0 cm), and thickness ($50 \pm 0.1(\text{RH})$ μm) of the Nafion 212 sample, respectively. As noted, the thickness is a function of water uptake,⁵⁴ and it varies from 53 to 59.5 μm for RH = 30 to 95%, respectively. The results of the ionic conductivity measurements for Nafion 212 as a function of RH at room temperature are shown in Figure 2. Interestingly, Nafion 212 shows ionic conductivity close to that of fully hydrated Nafion 112 at 100% relative humidity at 25 $^{\circ}\text{C}$ (vapor equilibrated).⁵⁴ The ionic conductivity of Nafion

212 increases exponentially with humidity, similar to that reported for Nafion 117.^{55,56}

3.2. Surface Ionic Conductivity Measurements. Figure 3 depicts the surface morphology, current-sensing images, surface-current

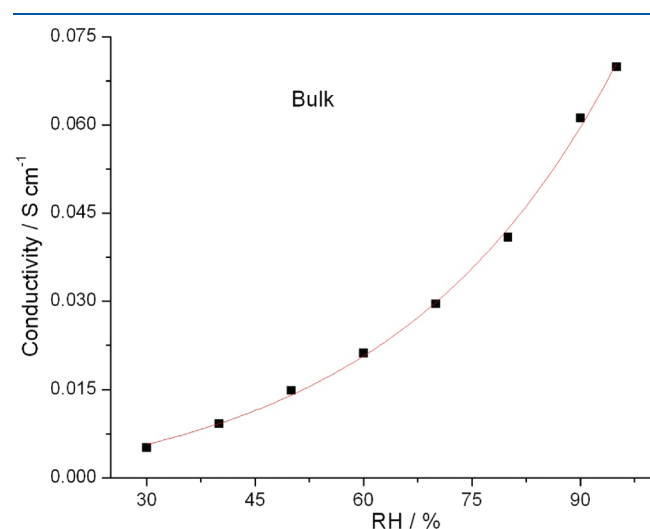


Figure 2. Influence of RH on the bulk conductivity of Nafion 212.

distribution, and low-current and high-current contour maps obtained from the current-sensing images of Nafion 212 for the RH range of 30–84% at room temperature. The topography images of Nafion 212 show a very inhomogeneous surface, although hydrophobic and hydrophilic domains composed of a fluorocarbon matrix and sulfonates cannot be distinguished. Close examination of the topography and current-sensing images does not reveal a correlation between the surface morphology and current images. Since the capacitive current due to charging of the AFM tip is negligible, and only current signals associated with electrochemical reactions can be detected, the variation in surface ionic conductance is directly related to the distribution of ionic clusters on the membrane surface.^{15,46} Thus, the current-sensing images shown in Figure 3 reflect the distribution of active ionic clusters on the surface and, to a certain extent, the percolated ion-conducting network in the membrane.

The CSAFM image of the membrane at RH = 30% (Figure 3B) shows large nonconductive regions responsible for the limited connectivity in the underlying hydrophilic network. As the RH increases to 51% and 65%, a more pronounced current pattern of more conducting and larger active regions is observed in CSAFM images. The clustering of hydrophilic domains proceeds further at 77% and 84% RH resulting in much larger ionically conducting areas on the membrane surface. However, a few nonconducting

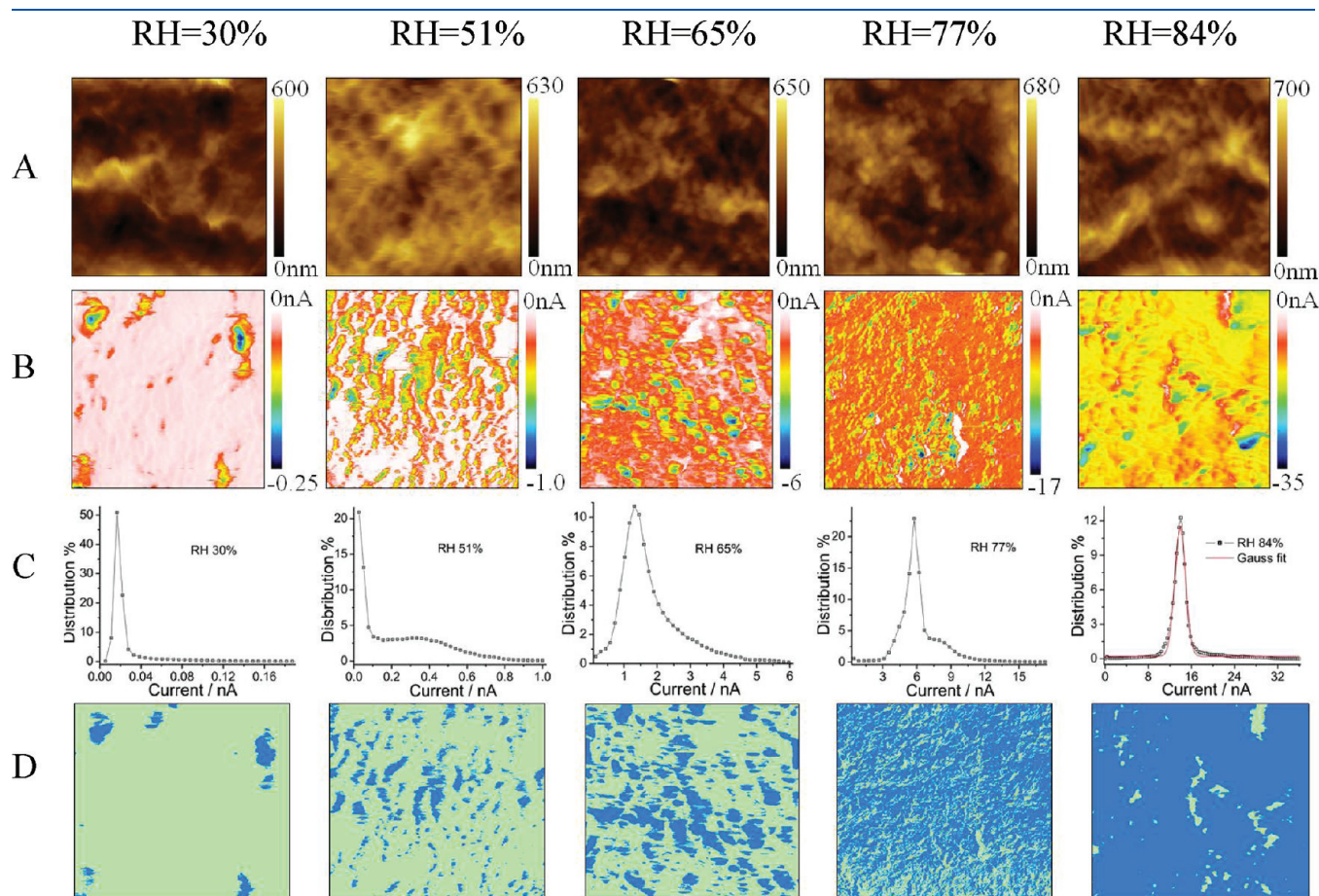


Figure 3. Synchronized AFM topography (row 1), current-sensing image (row 2), current distribution (row 3), and low-current (green) and high-current (blue) contour maps for current-sensing images (row 4) of Nafion 212 (bias voltage, -1.5 V; scan size, $5 \times 5 \mu\text{m}^2$; scan rate, 1 Hz). Column I: RH = 30%. Column II: RH = 51%. Column III: RH = 65%. Column IV: RH = 77%. Column V: RH = 84%. The red curves in the current distribution graph for RH = 84% indicate a Gaussian fit.

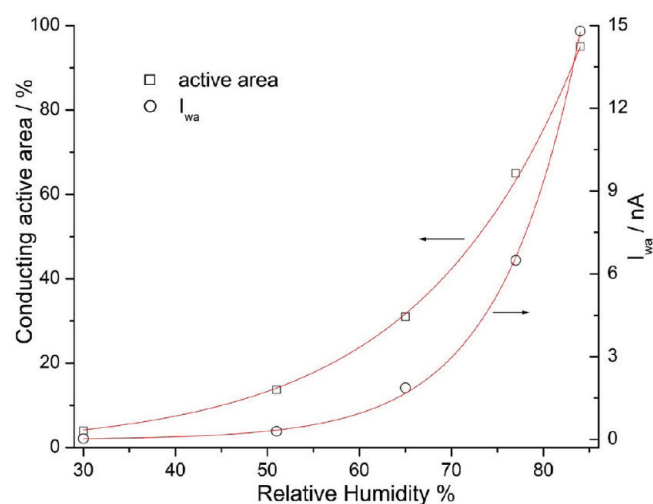


Figure 4. Influence of RH on the weighted-average current values of the conduction distributions and fraction of conducting active area from current-sensing images of Nafion 212.

spots, which are associated with the hydrophobic fluorocarbon phase, still remain on the membrane surface.

The surface-current distributions of Nafion 212 derived from the current-sensing images at different RH are depicted in Figure 3C. The ionic-current signal is determined by the contact area between the tip and the ionic clusters on the membrane surface.^{57,58} Consequently, the observed surface-current distribution reflects the average size of ionic clusters on the surface that are connected to the conductive network in the membrane bulk.

A plot of the weighted average current I_{wa} versus RH that is shown in Figure 4 exhibits an exponential dependence on humidity. Although the water meniscus may also increase the contact area between the tip and the ionic clusters due to water condensation at high RH, the primary contribution to the increased current value arises from the increased proton conductance through the ionic network in the membrane^{40,59} and the increased surface ionic conductivity (i.e., more ionic groups are available to facilitate proton transport through the membrane) when the membrane becomes more hydrated.^{31,59,60}

To determine the fraction of conducting active area (f_{aa}), the current-sensing images must be deconvoluted into conductive and nonconductive regions. Using a Gaussian fit for the current distribution at 84% RH in Figure 3C, the cutoff value (I_c) can be calculated from the first-standard-deviation value (σ') according to

$$\sigma' = \sqrt{\frac{1}{N}[(x_1 - \mu)^2 + (x_2 - \mu)^2 + \cdots + (x_N - \mu)^2]}$$

$$= 23.8 \text{ nA} \quad (3)$$

$$\mu = \frac{1}{N}(x_1 + \cdots + x_N)$$

$$I_c = I_{wa} - \sigma = 11.2 \text{ nA} \quad (4)$$

Unfortunately, the current distributions at the other RH values do not follow a Gaussian distribution. Therefore, the cutoff values are calculated using a cutoff ratio (R) obtained at 84% RH

$$R = I_c / I_m = 11.2 \text{ nA} / 35 \text{ nA} = 0.319 \quad (5)$$

Table 1. Current-Sensing AFM Results for Nafion 212 at Different Relative Humidities^a

RH	30%	51%	65%	77%	84%
I_{wa} (nA)	0.025	0.29	1.87	6.49	14.8
I_c (nA)	0.038	0.35	2.23	7.02	11.2
conducting active area %	4.1	13.7	30.9	65.2	94.8

^a I_{wa} : the weighted average of current distribution derived from topography and current-sensing images of a Nafion 212 membrane. I_c : the cutoff value for calculation of fraction of conductive area (f_{aa}).

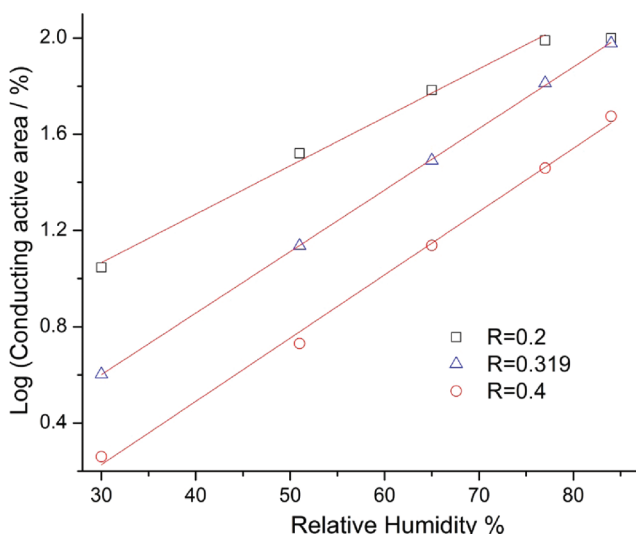


Figure 5. Influence of RH on the fraction of conducting active area values of a Nafion 212 sample with three cutoff ratio values.

where I_m is the maximum current value (35 nA) obtained from the CSAFM images.

The cutoff current (I_c) values were calculated for RH = 30%, 51%, 65%, and 77% and listed in Table 1. The resulting contour maps of the current-sensing images that consist of low-current regions (green) and high-current regions (blue) are shown in Figure 3D. In addition, the influence of RH on the fraction of ionically conductive area is plotted in Figure 4. An increase in the fraction of the membrane active area with humidity is consistent with earlier observations.³⁷ However, the fraction of conductive area of Nafion 212 increases exponentially as a function of RH, which is contrary to Aleksandrova's finding that the surface proton conductivity area of Nafion 112 is proportional to RH.³⁷ The difference between extruded Nafion 112 and dispersion-cast Nafion 212 can be attributed to differences in morphology and anisotropy of ionic channel networks.⁶¹

There still remains an open question that it might be arbitrary to assign the R value as 0.319. Choosing the right R value to calculate the fraction of conducting area is important for an accurate, quantitative characterization of the membrane surface. To examine this, we used alternative R values of 0.2 and 0.4 to calculate the fraction of conductive area for Nafion 212. From Figure 5, the exponential trend of the fraction of conductive area curve can be seen for all different R values ($R = 0.2, 0.319$, and 0.4). However, the results of fraction of conductive area using R values of 0.2 or 0.4 are inconsistent with the current-sensing images in Figure 3. For instance, using $R = 0.2$, the f_{aa} value for 77% RH has already

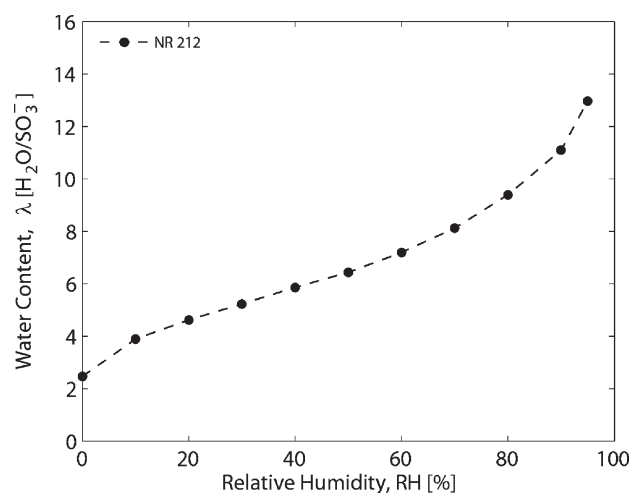


Figure 6. Sorption isotherm of Nafion 212 measured at 25 °C.

reached 99%, whereas Figure 3, row 2, column IV shows a large area of low-current domain.

To characterize accurately the effect of humidity on the ionic conductivity, RH values are converted to water content using the measured sorption isotherm from DVS analysis (Figure 6). The initial water content at 0% RH (λ_0) is around 2, indicating that a small amount of residual water exists in the membrane even under dry conditions. Figure 7 shows the fraction of active area, f_{aa} , as a function of water content, λ . The best fit to this data is obtained by a power-law scaling relationship, i.e.

$$f_{aa} \propto (\lambda - \lambda_0)^n \quad (6)$$

where the scaling exponent $n = 2.5$ and λ_0 is the initial water content. Our analysis suggests that actual water content in the membrane is a much better quantity than RH for correlating the membrane surface and bulk properties.

3.3. Correlating Fraction of Ionically Conductive Area to Mass Transport Properties. The ionically conductive areas on the membrane surface can be interpreted as the hydrophilic active sites comprising ion-rich water pools. Thus, ionic conductivity and water transport can be explored together to study the mechanisms of water and proton transport in the membrane. To understand better the role of the fraction of conducting area, i.e., concentration of hydrophilic sites on the surface, we use the water-vapor mass-transport coefficient, k_{int} , expressed as the reciprocal of the interfacial mass-transfer resistance⁵³ (Figure 7a).

$$N = k_{int}(a_{in} - a_{out}) \quad (7)$$

where N is the water flux through the interface, and a_{in} and a_{out} refer to the water activities directly inside and outside of the membrane interface, respectively. The interfacial mass-transfer resistance can be seen as a reciprocal resistance that is in series along with the transport resistance through the bulk membrane.

The resulting mass-transport coefficient increases (interfacial resistance decreases) with increasing water content, similar to the fraction of conducting area. Thus, the mass-transport coefficient can be correlated with the fraction of active area, the plot of which suggests a relationship of the form $k \propto f_{aa}^{1/2}$ (Figure 7b). Even though the findings here correlate and support the role of hydrophilic active sites in water transport, the definitive theoretical origins of this relationship require additional information on the

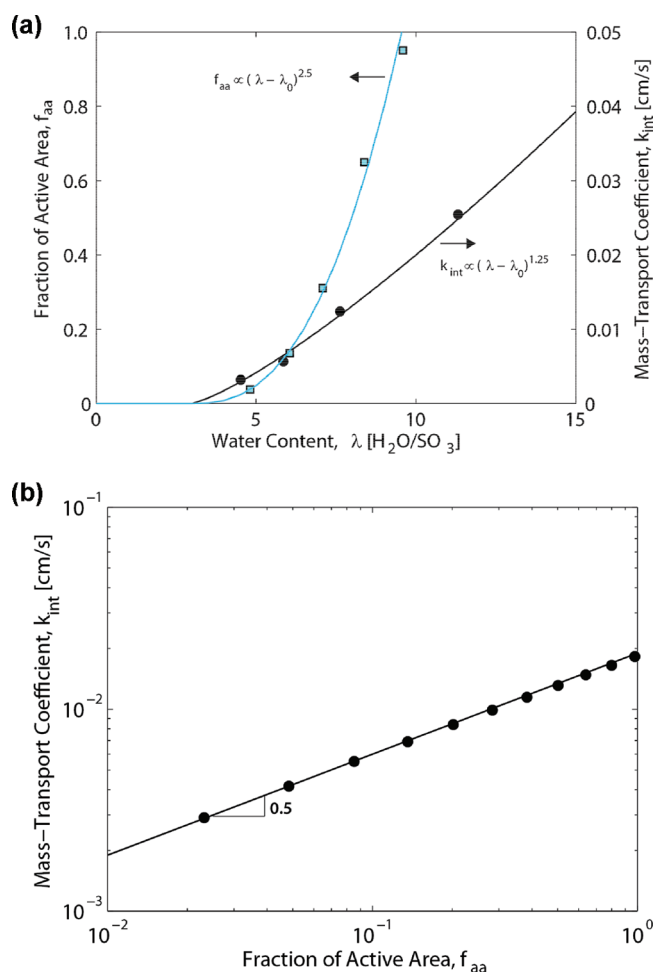


Figure 7. (a) Fraction of active area, f_{aa} , and mass-transport coefficient, k_{int} ,⁵³ as a function of water content for Nafion 212. (b) Correlation of the mass-transport coefficient with the fraction of active area for Nafion 212. Water-content values are determined from the relative humidities using the measured sorption isotherm (Figure 7).

surface morphology and membrane nanostructure, which is beyond the scope of this work.

To obtain an approximate measure of local ionic conductivity at the active sites, the average current is normalized with the fraction of active area, i.e., I_{aw}/f_{aa} , and plotted as a function of water content in Figure 8a. For comparison, measured bulk conductivity is also included along with an empirical fit. The scaling of bulk conductivity with water content can be written in the following empirical form based on percolation theory^{14,62}

$$\kappa \propto (\lambda - \lambda_0)^m \quad (8)$$

where λ_0 corresponds to the percolation threshold and the best-fit scaling exponent is $m = 1.57$, which is in accord with earlier studies on the conductivity of PFSA membranes.^{14,56,62,63} The above equation and percolation theory assume that at the percolation threshold a continuous water-filled transport network is formed across the membrane, and additional water makes the network less tortuous. Such an analysis is in concert with more complicated networks and transport derived from ab initio molecular dynamics for Nafion.⁶⁴ The normalized surface current and bulk ionic conductivity both exhibit a similar dependence on water content. By exploiting this similarity, the normalized surface

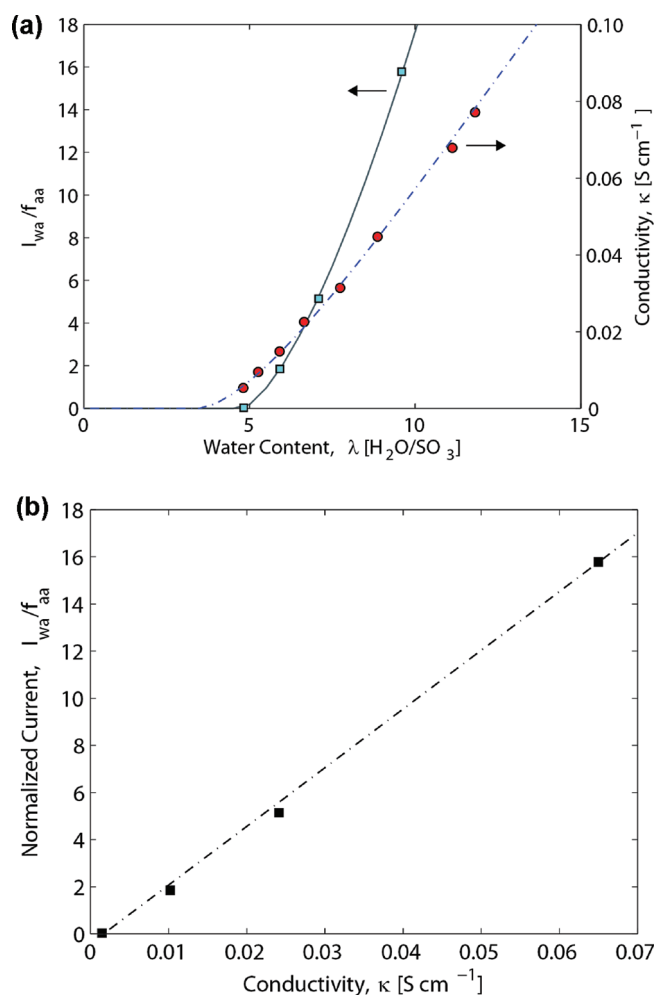


Figure 8. Comparison (a) and correlation (b) of normalized average current (with respect to the fraction of active area) and bulk conductivity of Nafion 212 at 25 °C.

current is plotted as a function of bulk conductivity (Figure 8b). Despite the limited data points, a very good linear correlation is observed, providing clear evidence for the relationship between the local and bulk conductivity.

3.4. Discussion. The accurate calculation of local ionic conductivity requires the contact area between the tip and the membrane, which is often challenging due to meniscus formation and a lack of knowledge about the meniscus shape and ionic conductivity. One can envision that a smaller meniscus may exhibit a higher ionic conductivity than a larger one due to its proximity to the sulfonic acid sites and their dissociation (i.e., Debye length), whereas the larger one has more bulk-like water. Because of the above ambiguities, we refrain from making quantitative comparisons between the local and bulk ionic conductivity. However, the linear relationship observed in Figure 8 can be used to investigate, at least qualitatively, how the ionically conducting sites on the membrane surface contribute to the bulk ionic conductivity. As humidity increases, additional hydrophilic sites form on the membrane surface, thereby facilitating the transport of water from the surface through the bulk membrane. In terms of proton conduction, this manifests itself as a contact resistance, where there are both highly conducting and nonconducting surfaces. Such a contact resistance has been shown to exist during ionic

conductivity measurements, and it is reported to decrease with increasing humidity in a nonlinear manner,⁶⁵ similar to the interfacial resistance for the water transport. The contact and water-mass-transfer resistances are very likely to be of the same origin that is controlled by the humidity-dependent surface structure of the membrane. Thus, increasing the fraction of hydrophilic phase at the membrane surface enhances the water transport and associated proton transport. However, it should also be noted that the strong correlation between the mass transport properties and fraction of surface ionically conducting area is relative in that the magnitudes of the mass-transfer coefficient and/or conductivity cannot be obtained unambiguously without a reference experimental measurement.

While the underlying mechanisms between water diffusion and proton conductivity may be different,^{14,66–68} they both require transport across the surface ionic sites. Thus, it is reasonable to focus on the morphology of the membrane surface to understand the local ionic conductivity. Bass and co-workers^{26,27} showed that the surface morphology of Nafion is strongly related to the humidity and interfacial effects. When the membrane faces a vapor phase below saturation, the surface ionic groups orient internal to the membrane/vapor interface to minimize interfacial energy, thereby reducing the surface fraction of the less-favored hydrophilic sites. The degree of this effect depends on humidity, with an inversion occurring in liquid water where the minimum interfacial energy is the case of the ionic groups oriented external to the membrane/vapor interface. This model is in accord with the observations of a higher fraction of conducting active area and improved surface current at higher humidities (Figure 7). Lastly, as the bulk conductivity requires the presence of active sites (e.g., SO_3 ionic groups) on the membrane surface, which have a direct role in local ionic conductivity, bulk conductivity is expected to increase linearly with the surface current as confirmed in Figure 8. Therefore, the slope of the line in that figure reflects the geometric features of the membrane nanostructure responsible for the proton movement, the understanding of which requires information on the three-dimensional morphology of the membrane from surface to inner regions.

4. CONCLUSIONS

We have studied the bulk and local ionic conductivities of a Nafion 212 membrane using direct-current voltammetry and current-sensing atomic force microscopy. CSAFM images of surface ionic conductivity and topography of Nafion 212 reveal that the surface-conductance variation is primarily correlated with the surface distribution of ionic clusters. The surface-current distributions of the membrane at different relative humidities reveal a nonlinear increase of the fraction of ionically conductive area with water content. The fact that the mass-transfer coefficient of the membrane, reflecting the resistance to water transport at the membrane–vapor interface, exhibits a similar dependence on humidity suggests that this resistance is controlled by the accessibility of the hydrophilic surface domains. Indeed, the mass-transfer resistance and fraction of conductive area can be simply correlated. Moreover, the increase in the bulk conductivity and surface current with water content are also correlated, where the bulk ionic conductivity is found to be directly proportional to the local ionic conductivity, suggesting that the limiting mechanisms of proton transport are similar in both cases. The reported information is of importance for understanding transport properties at the membrane surface and in its bulk and therefore allows

for the optimization of water management and performance in fuel cells.

AUTHOR INFORMATION

Corresponding Author

*E-mail: r_kostecki@lbl.gov.

ACKNOWLEDGMENT

This work was supported by the Assistant Secretary for Energy Efficiency and Renewable Energy, Office of Fuel Cell Technologies of the U.S. Department of Energy under Contract No. DE-AC02-05CH11231. We would like to thank Dr. Frank McLarnon for helpful comments and suggestions during preparation of this manuscript.

REFERENCES

- (1) Bai, H.; Ho, W. S. W. *Polym. Int.* **2011**, *60*, 26.
- (2) Cele, N.; Ray, S. S. *Macromol. Mater. Eng.* **2009**, *294*, 719.
- (3) Gasteiger, H. A.; Baker, D. R.; Carter, R. N.; Gu, W.; Liu, Y.; Wagner, F. T.; Yu, P. T. Electrocatalysis and catalyst degradation challenges in proton exchange membrane fuel cells. *Hydrogen Fuel Cells* **2010**, *3*.
- (4) Lim, B.; Yu, T.; Xia, Y. *Angew. Chem., Int. Ed.* **2010**, *49*, 9819.
- (5) Peckham, T. J.; Holdcroft, S. *Adv. Mater. (Weinheim, Ger.)* **2010**, *22*, 4667.
- (6) Stimming, U.; Jones, D.; Bele, P. *Fuel Cells (Weinheim, Ger.)* **2010**, *10*, 7.
- (7) Wannek, C.; Gluesen, A.; Stolten, D. *Desalination* **2010**, *250*, 1038.
- (8) Mauritz, K. A.; Moore, R. B. *Chem. Rev.* **2004**, *104*, 4535.
- (9) Zhang, L.; Mukerjee, S. *J. Electrochem. Soc.* **2006**, *153*, A1062.
- (10) Schlick, S.; Gebel, G.; Pineri, M.; Volino, F. *Macromolecules* **1991**, *24*, 3517.
- (11) Commer, P.; Cherstvy, A. G.; Spohr, E.; Kornyshev, A. A. *Fuel Cells (Weinheim, Ger.)* **2003**, *2*, 127.
- (12) Vishnyakov, A.; Neimark, A. V. *J. Phys. Chem. B* **2001**, *105*, 9586.
- (13) Gebel, G. *Polymer* **2000**, *41*, 5829.
- (14) Hsu, W. Y.; Gierke, T. D. *J. Membr. Sci.* **1983**, *13*, 307.
- (15) Hiesgen, R.; Aleksandrova, E.; Meichsner, G.; Wehl, I.; Roduner, E.; Friedrich, K. A. *Electrochim. Acta* **2009**, *55*, 423.
- (16) Bose, S.; Kuila, T.; Nguyen, T. X. H.; Kim, N. H.; Lau, K.-t.; Lee, J. H. *Prog. Polym. Sci.* **2011**, *36*, 813.
- (17) Takimoto, N.; Wu, L.; Ohira, A.; Takeoka, Y.; Rikukawa, M. *Polymer* **2009**, *50*, 534.
- (18) Morin, A.; Xu, F.; Gebel, G.; Diat, O. *Int. J. Hydrogen Energy* **2011**, *36*, 3096.
- (19) Fujimura, M.; Hashimoto, T.; Kawai, H. *Macromolecules* **1981**, *14*, 1309.
- (20) Elliott, J. A.; Hanna, S.; Elliott, A. M. S.; Cooley, G. E. *Macromolecules* **2000**, *33*, 4161.
- (21) Rubatat, L.; Rollet, A. L.; Gebel, G.; Diat, O. *Macromolecules* **2002**, *35*, 4050.
- (22) Kim, M. H.; Glinka, C. J.; Grot, S. A.; Grot, W. G. *Macromolecules* **2006**, *39*, 4775.
- (23) Fernandes, A. C.; Ticianelli, E. A. *J. Power Sources* **2009**, *193*, 547.
- (24) O'Dea, J. R.; Buratto, S. K. *J. Phys. Chem. B* **2011**, *115*, 1014.
- (25) James, P. J.; Elliott, J. A.; McMaster, T. J.; Newton, J. M.; Elliott, A. M. S.; Hanna, S.; Miles, M. J. *J. Mater. Sci.* **2000**, *35*, 5111.
- (26) Bass, M.; Berman, A.; Singh, A.; Kononov, O.; Freger, V. *J. Phys. Chem. B* **2010**, *114*, 3784.
- (27) Bass, M.; Berman, A.; Singh, A.; Kononov, O.; Freger, V. *Macromolecules* **2011**, *44*, 2893.
- (28) Malek, K.; Eikerling, M.; Wang, Q.; Liu, Z.; Otsuka, S.; Akizuki, K.; Abe, M. *J. Chem. Phys.* **2008**, *129*, 204702/1.
- (29) Schmidt-Rohr, K.; Chen, Q. *Nat. Mater.* **2008**, *7*, 75.
- (30) Slade, S. M.; Ralph, T. R.; Ponce de Leon, C.; Campbell, S. A.; Walsh, F. C. *Fuel Cells (Weinheim, Ger.)* **2010**, *10*, 567.
- (31) Anantaraman, A. V.; Gardner, C. L. *J. Electroanal. Chem.* **1996**, *414*, 115.
- (32) Peckham, T. J.; Schmeisser, J.; Holdcroft, S. *J. Phys. Chem. B* **2008**, *112*, 2848.
- (33) Peckham, T. J.; Schmeisser, J.; Rodgers, M.; Holdcroft, S. *J. Mater. Chem.* **2007**, *17*, 3269.
- (34) Fuller, T.; Uchida, H.; Strasser, P.; Shirvanian, P.; Lamy, C.; Hartnig, C.; Gasteiger, H. A.; Zawodzinski, T.; Jarvi, T.; Bele, P.; Ramani, V.; Cleghorn, S.; Jones, D.; Zelenay, P., Eds. Proton Exchange Membrane Fuel Cells 9. (Symposium held during the 216th Meeting of the Electrochemical Society in Vienna, Austria 4–9 October 2009). *ECs Trans.* **2009**, *25* (1), 2009.
- (35) Shevchenko, V. V.; Gumennaya, M. A. *Theor. Exp. Chem.* **2010**, *46*, 139.
- (36) Zawodzinski, T. A.; Gottesfeld, S.; Shoichet, S.; McCarthy, T. J. *J. Appl. Electrochem.* **1993**, *23*, 86.
- (37) Aleksandrova, E.; Hiesgen, R.; Friedrich, K. A.; Roduner, E. *Phys. Chem. Chem. Phys.* **2007**, *9*, 2735.
- (38) Van Nguyen, T.; Nguyen, M. V.; Lin, G.; Rao, N.; Xie, X.; Zhu, D.-M. *Electrochem. Solid-State Lett.* **2006**, *9*, A88.
- (39) Fan, F. R.; Bard, A. J. *Science (N.Y., NY)* **1995**, *267*, 871.
- (40) Xie, X.; Kwon, O.; Zhu, D.-M.; Nguyen Trung, V.; Lin, G. *J. Phys. Chem. B* **2007**, *111*, 6134.
- (41) Bath, B. D.; Lee, R. D.; White, H. S.; Scott, E. R. *Anal. Chem.* **1998**, *70*, 1047.
- (42) Bussian, D. A.; O'Dea, J. R.; Metiu, H.; Buratto, S. K. *Nano Lett.* **2007**, *7*, 227.
- (43) O'Hayre, R.; Lee, M.; Prinz, F. B. *J. Appl. Phys.* **2004**, *95*, 8382.
- (44) Kwon, O.; Wu, S.; Zhu, D.-M. *J. Phys. Chem. B* **2010**, *114*, 14989.
- (45) Kwon, O.; Wu, S.; Zhu, D.-M. *ECs Trans.* **2010**, *33*, 1035.
- (46) Aleksandrova, E.; Hiesgen, R.; Eberhard, D.; Friedrich, K. A.; Kaz, T.; Roduner, E. *ChemPhysChem* **2007**, *8*, 519.
- (47) Bass, M.; Freger, V. *Polymer* **2008**, *49*, 497.
- (48) Ge, S. H.; Li, X. G.; Yi, B. L.; Hsing, I. M. *J. Electrochem. Soc.* **2005**, *152*, A1149.
- (49) Majsztrik, P. W.; Satterfield, M. B.; Bocarsly, A. B.; Benziger, J. B. *J. Membr. Sci.* **2007**, *301*, 93.
- (50) Monroe, C. W.; Romero, T.; Merida, W.; Eikerling, M. *J. Membr. Sci.* **2008**, *324*, 1.
- (51) Satterfield, M. B.; Benziger, J. B. *J. Phys. Chem. B* **2008**, *112*, 3693.
- (52) Zhao, Q. A.; Majsztrik, P.; Benziger, J. *J. Phys. Chem. B* **2011**, *115*, 2717.
- (53) Kienitz, B.; Yamada, H.; Nonoyama, N.; Weber, A. Z. *J. Fuel Cell Sci. Technol.* **2011**, *8*, 011013.
- (54) Slade, S.; Campbell, S. A.; Ralph, T. R.; Walsh, F. C. *J. Electrochem. Soc.* **2002**, *149*, A1556.
- (55) Mura, F.; Silva, R. F.; Pozio, A. *Electrochim. Acta* **2007**, *52*, S824.
- (56) Morris, D. R.; Sun, X. D. *J. Appl. Polym. Sci.* **1993**, *50*, 1445.
- (57) Kang, Y.; Kwon, O.; Xie, X.; Zhu, D.-M. *J. Phys. Chem. B* **2009**, *113*, 15040.
- (58) Kwon, O.; Kang, Y.; Wu, S.; Zhu, D.-M. *J. Phys. Chem. B* **2010**, *114*, 5365.
- (59) Choi, P.; Jalani, N. H.; Datta, R. *J. Electrochem. Soc.* **2005**, *152*, E84.
- (60) Rollet, A.-L.; Diat, O.; Gebel, G. *J. Phys. Chem. B* **2002**, *106*, 3033.
- (61) Li, J.; Wilmsmeyer, K. G.; Madsen, L. A. *Macromolecules (Washington, DC, U. S.)* **2009**, *42*, 255.
- (62) Weber, A. Z.; Newman, J. J. *Electrochem. Soc.* **2004**, *151*, 311.
- (63) Edmondson, C. A.; Fontanella, J. J. *Solid State Ionics* **2002**, *152*, 355.

- (64) Hwang, G. S.; Kaviani, M.; Gostick, J. T.; Kienitz, B.; Weber, A. Z. *Polymer* **2011**, *52*, 2584.
- (65) Cooper, K. *ECS Trans.* **2009**, *25*, 995.
- (66) Kreuer, K. D.; Weppner, W.; Rabenau, A. *Solid State Ionics* **1981**, *3–4*, 353.
- (67) Zawodzinski, T. A.; Neeman, M.; Sillerud, L. O.; Gottesfeld, S. *J. Phys. Chem.* **1991**, *95*, 6040.
- (68) Kreuer, K. D. *Solid State Ionics* **1997**, *94*, 55.